Defence Technology 35 (2024) 47–59

Contents lists available at ScienceDirect

Defence Technology

journal homepage: www.keaipublishing.com/en/journals/defence-technology

Influence of manufacturing process-induced geometrical defects on the energy absorption capacity of polymer lattice structures

Alexandre Riot [a, b], Enrico Panettieri [a], Antonio Cosculluela [b], Marco Montemurro [a, *]

[a] Université de Bordeaux, Arts et Métiers Institute of Technology, CNRS, INRA, Bordeaux INP, HESAM Université, I2M UMR 5295, F-33405 Talence, France
[b] French Atomic Energy Commission, Route des Gargails, Cedex, F-33114, Le Barp, France

ARTICLE INFO

Article history:
Received 2 December 2022
Received in revised form
8 July 2023
Accepted 6 September 2023
Available online 9 September 2023

Keywords:
Lattice structures
Architected cellular materials
Dynamic simulation
Energy absorption
Geometrical imperfection
Additive manufacturing

ABSTRACT

Modern additive manufacturing processes enable fabricating architected cellular materials of complex shape, which can be used for different purposes. Among them, lattice structures are increasingly used in applications requiring a compromise among lightness and suited mechanical properties, like improved energy absorption capacity and specific stiffness-to-weight and strength-to-weight ratios. A dedicated modeling strategy to assess the energy absorption capacity of lattice structures under uni-axial compression loading is presented in this work. The numerical model is developed in a non-linear framework accounting for the strain rate effect on the mechanical responses of the lattice structure. Four geometries, i.e., cubic body centered cell, octet cell, rhombic-dodecahedron and truncated cuboctahedron 2+, are investigated. Specifically, the influence of the relative density of the representative volume element of each geometry, the strain-rate dependency of the bulk material and of the presence of the manufacturing process-induced geometrical imperfections on the energy absorption capacity of the lattice structure is investigated. The main outcome of this study points out the importance of correctly integrating geometrical imperfections into the modeling strategy when shock absorption applications are aimed for.

1. Introduction

In several industrial sectors, the mechanical response of structures under dynamic loads is usually investigated to assess and validate specific design requirements, such as impact resistance, payload protection or quasi-static load withstanding. In the case of impacts, shock absorbers are used to absorb a maximum amount of impact energy, minimizing the protected load probability of being structurally compromised by any violent collision. According to Refs. [1], shock absorbers are the main relevant protection architecture ensuring sensitive material or people safety by being subject to progressive local strain, as a mean to minimize permanent damage. These absorbers roles are commonly filled by cellular solids-void cells interconnected with solid shells or beams. Cellular solids are assorted into two typologies of structures. The first class includes stochastic cellular structures, which are open or closed cells of random spatial distribution and sizes but assumed as homogeneously distributed in a statistically representative volume element (RVE). The second class includes periodic cellular structures, which are open or closed geometries, identical in size and shape, distributed according to a periodic pattern at the macroscopic scale.

Stochastic cellular structures may be subdivided into two categories [1]: closed cell stochastic solids or open cells stochastic solids. Closed cellular solids, such as agglomerated cork, have consistent force attenuation properties, inversely proportional to the specimen thickness, high energy absorption capacities, which are preserved even after impact phenomena (from 70% to 80%) [2,3], and, consequently, are suitable candidates for vehicle seats, high speed helmets [4] and even for composite sandwich structures for military and aerospace applications [5]. Open cellular solids, such as polymeric foams, present the same advantages as their closed cell counterparts [6], although used for lower strain-rate applications and vibration damping [7], as these foams are not suited for personal protection such as helmets [8]. These cellular structures present a major

* Corresponding author.
E-mail addresses: marco.montemurro@ensam.eu, marco.montemurro@u-bordeaux.fr (M. Montemurro).
Peer review under responsibility of China Ordnance Society

https://doi.org/10.1016/j.dt.2023.09.003

weakness that has direct consequences on the mechanical behavior: the uncontrolled presence of local imperfections in the micro and meso-structure, such as bubbles or inner grain mantles [9], due to the manufacturing process. Specifically, foams tend to have enhanced mechanical properties along the foam rising direction [10]. Therefore, when incorporated into larger structures, the stochastic architectures might present unexpected mechanical behavior, tailoring forces in uncontrolled directions.

In analogy with stochastic cellular structures, periodic cellular structures may be subdivided into the same two families. Some periodic structures are suited to tailor loads in specific directions. For example, honeycombs are suitable for loads following the direction of honeycomb extrusion [11–14] and exhibit anisotropic behavior in the two other loading directions [15]. For other periodic cellular structures, like lattice structures (LSs), the mechanical behavior is strongly dependent on the RVE geometry [16–23] and on relative density [24] or less influenced by the cell size [25]. Extended studies indicate that the use of LSs is crucial to achieve an optimal level of energy absorption capacity (EAC) for specific load cases [26,27]. Moreover, experimental data suggest that the increase of the number of cells in a fixed absorber volume tends to stabilize and increase the levels of absorbed energy, although this assessment has yet to be numerically validated [28]. Regarding the mechanical behavior and EAC of regular cubic and functionally graded lattice structures under uniaxial quasi-static loads, consequent groundwork has been established [29–32]. Specifically, dynamic simulations to assess the mechanical behavior of honeycomb panels have been carried out thoroughly, indicating relative density plays a significant role in the EAC of periodic cellular structures, and putting forward the importance of the RVE geometrical features in structural collapse and load tailoring [33,34]. Currently, additive manufacturing (AM) processes for polymers enable the possibility of fabricating such structures, as discussed inRefs. [35–37]. However, processes such as Stereolithography Apparatus (SLA), Continuous Liquid Interface Production (CLIP) or Digital Light Synthesis (DLS) present high resolution capacities, down to an in-plane resolution of 25 μm, and indistinguishable layers of material in the vertical direction, generating a bulk material characterized by an essentially isotropic behavior, which reduces the sources of errors when modeling the constitutive behavior in finite element (FE) analyses [38,39]. Nevertheless, geometrical imperfections due to AM processes, such as curling or trapezoid deformations [40,41], must be considered when designing structural components made of LSs. Simulations to assess the influence of geometrical imperfections on the mechanical response of the structure have been carried out in Refs. [42,43], limiting the study to linear elastic material properties.

In this context, the aim of this paper is to propose a general numerical strategy to evaluate the influence of geometrical imperfections induced by the manufacturing process on the EAC of LSs in non-linear dynamic analyses, considering both the non-linear strain-rate dependent constitutive material model and the contact interactions between the geometrical features of the RVE of the LS. Four RVE geometries belonging to the class of strut-based LSs [44,45] have been selected and investigated in this paper. For each configuration, an extensive campaign of sensitivity analyses of the EAC to the value of the RVE relative density as well as to the macroscopic compressive strain rate is carried out. Furthermore, the influence of geometrical imperfections on the EAC is studied by considering different parameters that contribute to the definition of the deformed shape: the maximum value of the defect size and the shape of the imperfection.

The remainder of the paper is as follows. The problem description is given in Section 2, while Section 3 presents the RVE geometries analyzed in this work as well as the constitutive law of the bulk material. The numerical framework developed to address the mechanical problem is presented in Section 4 together with the details of the sensitivity analyses. The numerical results are presented and discussed in Section 5, while meaningful conclusions and prospects are provided in Section 6.

2. Description of the mechanical problem

To evaluate the capability of cellular structures to absorb energy under impact loads, two indicators are usually assumed in experiments [46]: the EAC, which considers the area under the local stress vs. nominal strain measurements and the energy absorption efficiency (EAE), which is computed as the ratio of the EAC to the maximum nominal compressive stress. Both indices are considered applicable before densification of the cellular structural configuration occurs and under the hypothesis that, during the application of the external load, the strain rate is kept constant. The comparison between cellular structures made of different bulk materials and different relative densities can be performed by normalizing the value of the EAC by both the value of relative density and bulk material density. The normalized EAC, $\overline{W}_c$ can be computed as:

$$\overline{W}_c(\epsilon) = \frac{1}{\overline{\rho}\rho_{mat}} \int_0^{\epsilon_f} \sigma_c d\epsilon = \frac{W_c}{\overline{\rho}\rho_{mat}}, \tag{1}$$

where $\overline{\rho}$ is the relative density, ρ_{mat} is the density of the bulk material of the RVE, σ_c is the compressive stress obtained from the experiments as the ratio of the load cell force to the initial specimen section and ϵ_f is the compressive strain before densification occurs computed as the ratio of the applied compressive displacement to the initial specimen height.

In the context of the current numerical study, the indicator used to quantify the energy absorption of cellular structures under dynamic loading is the normalized internal energy $\overline{IE}$, which is more suited to the analysis of numerical results if compared to the normalized EAC indicator. For a general loading condition, the normalized internal energy of a body can be computed as:

$$\overline{IE}(\epsilon) = \frac{IE(\epsilon)}{\overline{\rho}\rho_{mat}} = \frac{E_e + E_p + E_v}{\overline{\rho}\rho_{mat}}, \tag{2}$$

where $\overline{IE}(\epsilon)$ is the internal energy computed for the whole body volume, E_e is the elastic strain energy, E_p is the energy dissipated via plasticity, E_v is the energy dissipated by time-dependent mechanisms (e.g., viscosity).

The value of $\overline{IE}$ can be obtained by computing the terms E_e, E_p and E_v as follows:

$$\overline{IE}(\epsilon) = E_e + E_p + E_V = \int_0^t \left(\int_V \sigma : \dot{\epsilon}_e dV \right) d\tau + \int_0^t \left(\int_V \sigma : \dot{\epsilon}_p dV \right) d\tau + \int_0^t \left(\int_V \sigma : \dot{\epsilon}_v dV \right) d\tau, \tag{3}$$

where σ is the stress tensor and $\dot{\epsilon}_e$, $\dot{\epsilon}_p$ and $\dot{\epsilon}_v$ are the three strain rate tensors which describe the contributions to the total strain rate tensor decomposition, i.e.,

$$\dot{\epsilon} = \dot{\epsilon}_e + \dot{\epsilon}_p + \dot{\epsilon}_v, \tag{4}$$

where $\dot{\epsilon}_e$ is the elastic strain rate tensor, $\dot{\epsilon}_p$ is the plastic strain rate tensor and $\dot{\epsilon}_v$ is the strain rate tensor related to time-dependent mechanisms.

In the following of this paper, the quantity $\overline{IE}$ is used to perform a comparative study on the dynamical behavior of four lattice

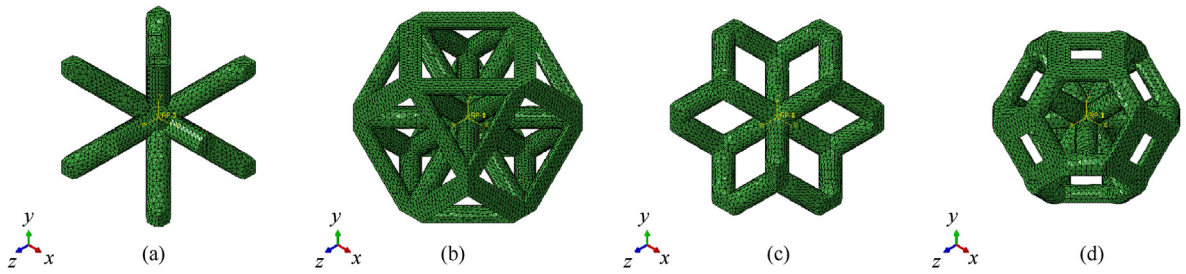

Fig. 1. Geometries of the lattice structures considered in this study: (a) CBCC; (b) OC; (c) RD; (d) TrCO.

configurations characterized by different values of relative density and different values of applied strain rate in the presence of geometrical imperfections aimed at reproducing those typically related to AM technology. Finally, a comparison between the $\overline{IE}$ and the $\overline{W}_c$ indicators is systematically carried out on selected RVE configurations to highlight and discuss their fitness to address the mechanical response of LSs in shock absorption applications.

3. Geometry and material properties

Four RVE geometries embedded in a cubic domain have been selected for this study. They have been taken from Ref. [20] and shown in Fig. 1: cubic body centered configuration (CBCC), octet configuration (OC), rhombic-dodecahedron (RD) and truncated cuboctahedron 2+(TrCO). Three values of relative density $\overline{\rho}$, defined as the ratio of the volume occupied by the bulk material to the volume of the whole RVE, have been considered: $\overline{\rho} = [0.2, 0.4, 0.6]$.

Due to the cubic volume of the RVE, only two geometrical parameters are needed to define the lattice architecture: the global cell size L_c, and the radius of the struts R_a, as illustrated in Fig. 2(a). The relationship $\overline{\rho}\ (L_c, R_a)$ between the relative density and the geometrical parameters L_c and R_a, has been determined through preliminary geometric/numerical analyses. As a result, Fig. 2(b) shows the four surfaces describing the function $\overline{\rho}\ (L_c, R_a)$ for each RVE geometry. The four solid lines of Fig. 2(b) represent the intersection between the fitting surfaces and the horizontal plane, $\overline{\rho}\ (L_c, R_a) = 0.2$. The solid lines are then used to define the relationships between the geometrical parameters L_c and R_a which are needed to generate the FE model of the lattice geometry characterized by the selected relative density.

The analytical relationships that define the curves resulting from the intersection between the fitting surfaces and the horizontal planes at $\overline{\rho}\ (L_c, R_a) = [0.2, 0.4, 0.6]$ can be properly interpolated with a linear relationship as follows:

$$L_c(\overline{\rho}) = C(\overline{\rho})R_a \tag{5}$$

where the coefficients $C(\overline{\rho})$ are provided in Table 1 for each RVE geometry.

The bulk material constituting the lattice cells is a Thermoplastic Polyurethane (TPU). The constitutive behavior of the TPU, typically assumed as hyper-viscoelastic [47], is modeled via a Cowper-Symonds (CS) material model [48], which represents a relatively simple material model capable to reproduce an elasto-plastic constitutive law including strain rate-dependency hardening effects. In the CS model, the flow stress σ_y is described via a power law as follows:

$$\sigma_y = \sigma_y^{QS}\left[1 + \left(\frac{\dot{\varepsilon}}{D}\right)^{\frac{1}{p}}\right], \tag{6}$$

where the flow stress values at a given strain-rate value $\dot{\varepsilon}$ is computed by scaling the quasi-static yield stress values σ_y^{QS} obtained via quasi-static compression tests on the bulk material, with a power law relationship characterized by two parameters, D and p, to be determined via dedicated experimental dynamic tests.

The set of parameters describing the CS material model, used in the present study, is reported in Table 2. The $\sigma-\varepsilon$ curves corresponding to the three strain-rate values $\dot{\varepsilon} = [250, 750, 1250]\ s^{-1}$ considered for the sensitivity analyses discussed in section 4 are shown in Fig. 3 together with the quasi-static $\sigma-\varepsilon$ data (black markers in Fig. 3), taken from Ref. [48], from which the corresponding quasi-static constitutive law has been approximated.

4. The numerical modeling strategy

4.1. The finite element model of the representative volume element

The campaign of sensitivity analyses presented in this work aims to investigate the sensitivity of the dynamical response of the RVE geometries shown in Fig. 1 to the following parameters:

- The relative density of the RVE.
- The value of the strain rate imposed to the RVE.
- The geometrical imperfections resulting from the manufacturing process.

Three values of relative densities are considered in all the analyses, i.e., $\overline{\rho} = [0.2, 0.4, 0.6]$, for which three values of strain rate, i.e., $\dot{\varepsilon} = [250, 750, 1250]s^{-1}$, are used to define the dynamic compressive loading.

To evaluate the EAC of the different RVE geometries and to assess the influence of manufacturing-induced geometrical imperfections on the dynamics of the LS, a numerical framework is developed within the Abaqus® FE commercial software.

Python scripts are created and coupled with the Abaqus CAE interface to perform all the operations required to prepare the input files to be submitted to the Abaqus Implicit solver. An example of the FE model, for each RVE topology, is illustrated in Fig. 1. Specifically, for each RVE geometry, the following operations have been completely automated: (1) creation of one eighth of the RVE geometry; (2) creation of the mesh and generation of the FE model of the whole RVE by means of duplication and mirroring operations; (3) applications of the periodic boundary conditions (PBCs) to the boundary of the FE model (this operation is carried out through the HOMTOOLS[1] toolbox for Abaqus); (4) definition of the contact regions (contact zone between the struts composing the RVE, including self-contact) and of the loading case (i.e., uni-axial stain field along x axis); (5) submission of the run and post-processing of the results.

The first two operations allow obtaining a perfect matching of

[1] http://homtools.lma.cnrs-mrs.fr/

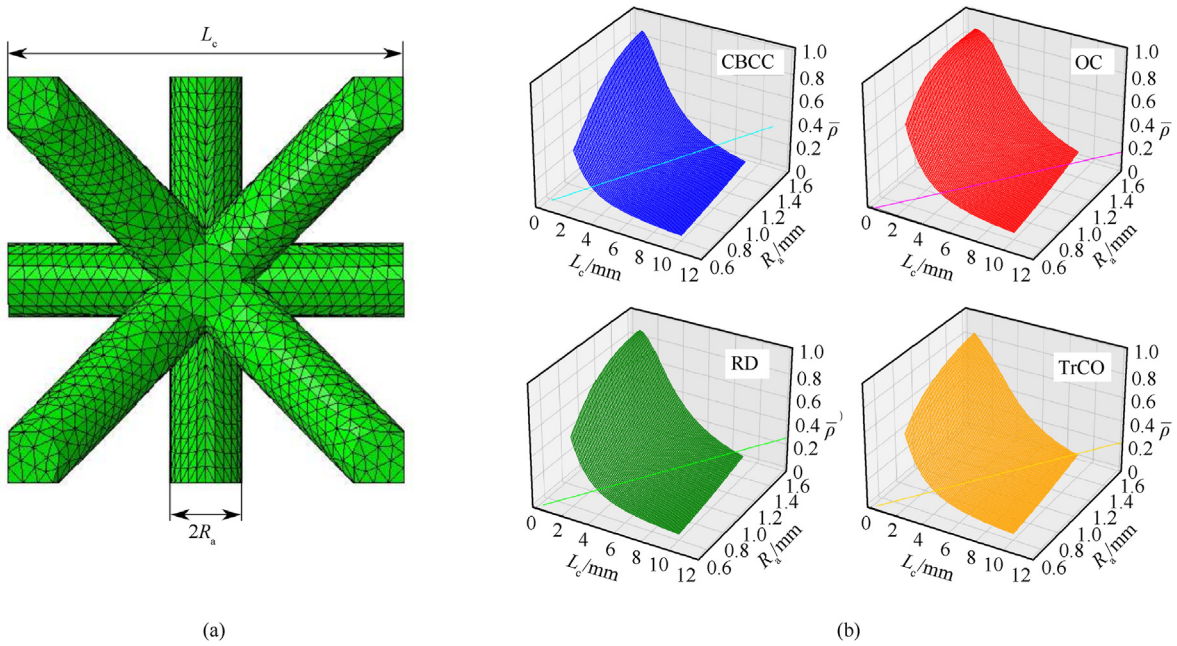

Fig. 2. (a) Geometrical parameters of the lattice cells; (b) Relative density as function of the two geometrical parameters.

Table 1
Values of the coefficient of the linear interpolation law relating the geometric parameters of the cubic RVE at the selected values of relative density.

	CBCC	OC	RD	TrCO
$C(\bar{\rho}=0.2)$	5.49	7.28	6.47	6.702
$C(\bar{\rho}=0.4)$	3.69	4.74	4.27	4.394
$C(\bar{\rho}=0.6)$	2.94	3.71	3.36	3.449

Table 2
TPU material properties for the definition of the Cowper-Symonds material model.

Property	Value	Plastic strain	Yield stress/MPa
Young Modulus, E_{TPU}/MPa	158	0	11.05
Poisson coefficient, ν_{TPU}	0.4	0.36	25.92
Density, ρ_{TPU} /(kg•m^{-3})	1150	0.76	45.36
Cowper-Symonds law parameter		1.42	119.02
Value			
D/s^{-1}	971	1.90	265.26
p	0.98	2.18	295.46
		2.97	390.17

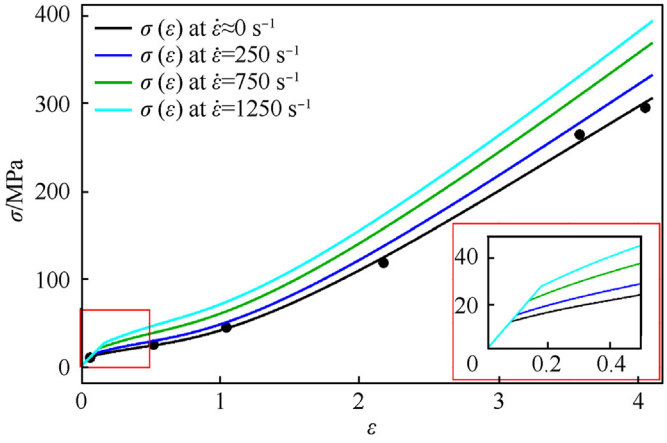

Fig. 3. Stress-strain curves obtained with the Cowper-Symonds material model: black dots represent the experimental data taken from Ref. [48] and provided in Table 2. Solid black line is obtained by fitting the shown experimental data.

those nodes located on opposite sides of the FE model, which is needed for the PBCs to be correctly enforced [49]. Although the maximum compressive strain is set equal to 0.4, for all the RVE geometries considered in the study, the value of the constant strain rate is set by acting on the simulation time t_{sim} as follows:

$$t_{sim} = \frac{\varepsilon_{max}}{\dot{\varepsilon}},\ \varepsilon_{max} = 0.4,\ \dot{\varepsilon} = [250, 750, 1250]\text{s}^{-1} \quad (7)$$

The value of t_{sim} obtained from Eq. (7) defines the step time of the implicit dynamic non-linear analysis.

Due to the complexity of the geometries at hand, four-node tetrahedral elements (C3D4) [50] are used to generate the FE model with a total number of elements of approximately 240000 (different RVE geometries and relative densities are characterized by a different number of elements). To prevent interpenetration and meaningless deformed shape of the struts constituting the RVE geometry during compression, general contact interaction with penalization is enforced to all the external element faces. Moreover, frictionless contact interactions have also been added between the external element faces of the lattice FE model and two rigid planes, as shown in Fig. 4. These planes, placed in proximity of the FE model, follow the lattice FE model external faces along the global x-axis (the loading direction) as illustrated in Fig. 4. The aim of the rigid planes is twofold. On the one hand, they allow to enforce the periodicity of the deformation of those regions of the FE model of the RVE which are not driven via the PBCs (i.e., nodes belonging to struts that do not lie on the model boundaries). On the other hand, they allow simulating the presence of adjacent cells and, thus, the occurring of the densification phenomenon (which cannot be predicted when considering the FE model of single RVE).

Of course, by including the rigid planes within the simulations, the value of the EAC will increase, as expected, for all the sensitivity analyses due to the additional lateral confinement, which generates higher stress/strain values in the struts of the RVE involved in the

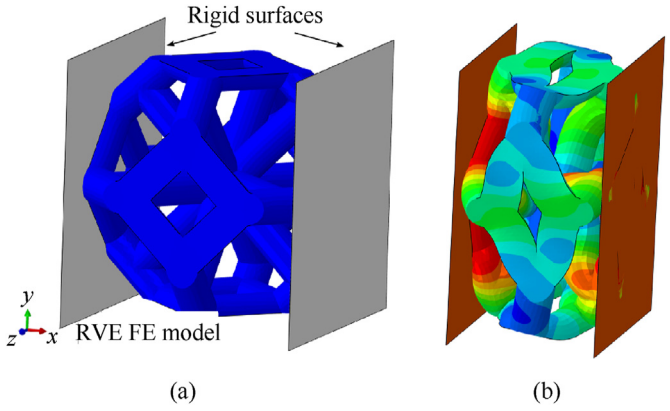

Fig. 4. (a) Numerical analysis setup with rigid surfaces to reproduce densification effects at high strain values of uniaxial strain; (b) Example of a deformed configuration of the TrCO cell for $\overline{\rho} = 0.2$ at $\varepsilon = \varepsilon_{max} = 0.4$. The color plot corresponds to that of the magnitude of the displacement vector.

contact (which takes place at high values of the imposed macroscopic strain when densification occurs). Fig. 5 shows a comparison between both the force vs. deformation curves obtained for the TrCO geometry, at different values of relative density, with and without rigid surfaces and the deformed shapes of the same RVE geometry at $\varepsilon = \varepsilon_{max} = 0.4$.

Due to the significantly greater computational cost of numerical analyses including contact interactions with the rigid planes, a preliminary evaluation of the EAC has been carried out on all the RVE geometries with and without rigid planes. For all the considered RVE configurations, except to the TrCO topology, the relative difference of the EAC assessed with and without modeling rigid planes is negligible. Therefore, rigid planes have been included within all the numerical analyses of the TrCO RVE geometry which, as discussed later in subsection 5.2, is the one capable of absorbing more energy when geometrical defects are considered, if compared to the other RVE geometries. It stands out that, for the TrCO RVE geometry, the relative error of the EAC between the simulations without rigid planes and those with rigid planes spans is, in any case, between 3% and 10%. To this purpose, it was not considered relevant to include the contact interactions with the rigid planes within the numerical analyses for the three other RVE geometries (CBCC, OC and RD).

A preliminary sensitivity analysis of the EAC to the mesh size is performed to identify the value of the average element size allowing for a reasonable compromise between accuracy of the results of the non-linear analyses and computational costs. As an example, Fig. 6 points out the influence of the average element size (e_{size}) on the normalized compressive force vs. the macroscopic strain imposed to a CBCC geometry characterized by a relative density $\overline{\rho} = 0.2$ at a strain rate $\dot{\varepsilon} = 750\ s^{-1}$. The results of these preliminary analyses point out that an average element size of approximately 0.4 mm allows for a good compromise between accuracy of the results and computational cost, as shown in Fig. 6, in terms of normalized compressive effort, normalized simulation time and normalized strain energy. The normalization is performed with respect to the relevant quantities obtained for the coarsest average element size ($e_{size} = 0.46$ mm). It results that a value of $e_{size} = 0.39$ mm represents a good compromise between simulation time and accuracy in assessing the normalized strain energy.

4.2. Description of the sensitivity analyses

To quantify the influence of geometrical imperfections on the capacity of the considered lattice cells to absorb energy, a systematic sensitivity analysis is carried out. Different scenarios of geometrical imperfections are imposed to the considered RVE geometries and the resulting values of absorbed energy are compared with those obtained on idealized RVE geometries (i.e., without defects) for different values of both macroscopic strain rate and relative density.

Different approaches can be used to introduce geometrical imperfections in a FE model. For instance, one can introduce a random offset to the coordinates of each node constituting the FE model, or an analytical definition of the imperfection can be used to define the initial configuration of the FE model. A sound alternative consists in introducing a linear combination of the normalized displacement fields related to the first N buckling loads (i.e., the deformed shapes corresponding to the eigen-vectors) to generate a global imperfection. The latter approach is usually used in the context of post-buckling analyses of structures [51–53] and it has

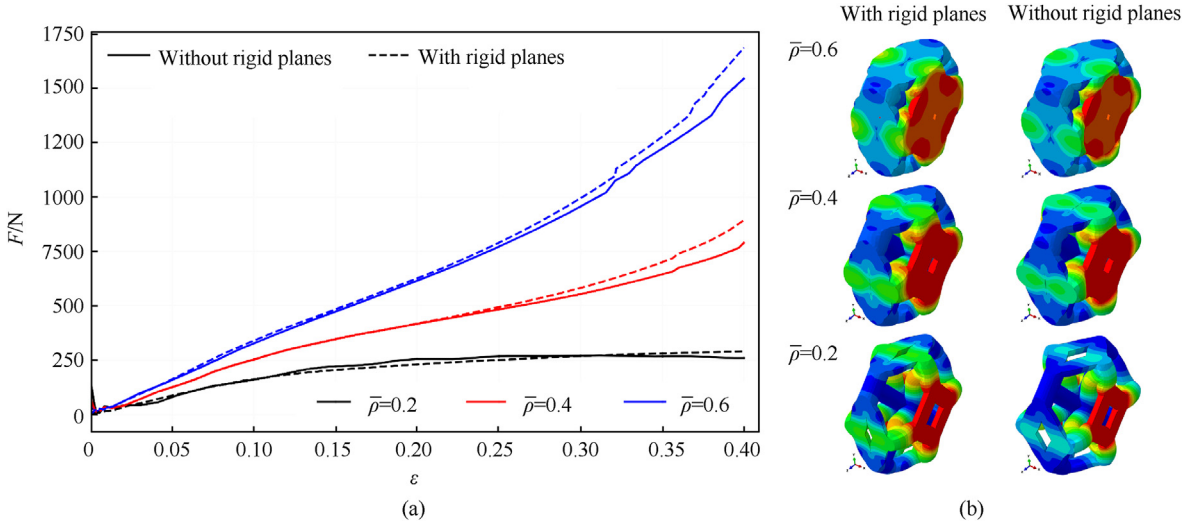

Fig. 5. (a) Longitudinal force vs. longitudinal deformation curves of the TrCO geometry for $\overline{\rho} = [0.2, 0.4, 0.6]$ and $\dot{\varepsilon} = 750\ s^{-1}$ with and without rigid planes; (b) Comparison of the deformed shapes at $\varepsilon_{max} = 0.4$ of the simulations performed with and without rigid surfaces at $\dot{\varepsilon} = 750\ s^{-1}$ (rigid surfaces have been hidden to show the lattice cell). The color plot corresponds to that of the displacement magnitude.

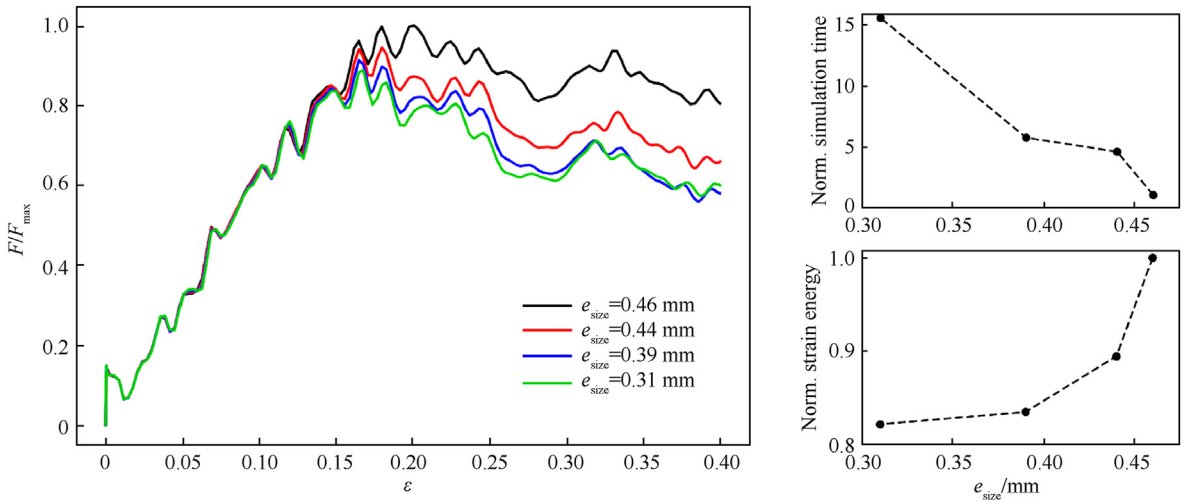

Fig. 6. Example of the sensitivity of the results of the non-linear dynamic analysis to the average element size on the CBCC geometry for $\bar{\rho} = 0.2$ and $\dot{\varepsilon} = 750\ s^{-1}$: normalized longitudinal force vs. macroscopic longitudinal strain, normalized simulation time vs. average element size and normalized strain energy vs. average element size. The curves have been obtained for one of the simulation scenario discussed in subsection 4.2 including a geometrical imperfection.

been applied in the present study.

Once the normalized nodal displacements of the FE model of the RVE are extracted from eigenvalue buckling analyses, the global imperfection is generated by changing the coordinates of the nodes of the RVE as follows:

$$\boldsymbol{u}(x) = \sum_{i=1}^{N} \left(\varphi_i \boldsymbol{u}_i^0(x) \right), \tag{8}$$

where $\boldsymbol{u}(x)$ is the nodal displacement vector which define the global imperfection to be imposed to the FE model (x contains the nodal coordinates), N is the number of buckling modes included in the definition of the global imperfection, φ_i is the value of the weight coefficient associated to the i-th buckling mode and $\boldsymbol{u}_i^0(x)$ is the normalized nodal displacement vector of the i-th buckling mode.

Eq. (8) shows that, for a generic FE model, two parameters influence the global imperfection: the number of modes N and the weights φ_i. In the present study, the weight coefficients are the same for each buckling mode included within the global imperfection. As a consequence, once the maximum global amplitude is defined, the weight coefficients are computed by dividing the global amplitude by the number of modes N. As an example of typical buckling modes obtained for the studied lattice cells, Fig. 7 shows the buckling modes of the considered RVE geometries relative to modes number 3, 6 and 8.

Table 3 lists the scenarios considered in the campaign of sensitivity analyses presented in this work. These scenarios aim at addressing the influence of different parameters defining the geometrical imperfection on the EAC of each RVE topology. Particularly, two aspects are addressed: the choice of the buckling modes which define the global imperfection (scenarios D1 and D2) and the absolute value of the global amplitude of the geometrical imperfection (scenario D3). Finally, the effect of the lattice cell relative density is addressed in scenario D4. The value of the global amplitude defining the imperfection is provided as a percentage value of the RVE size $2L_c$.

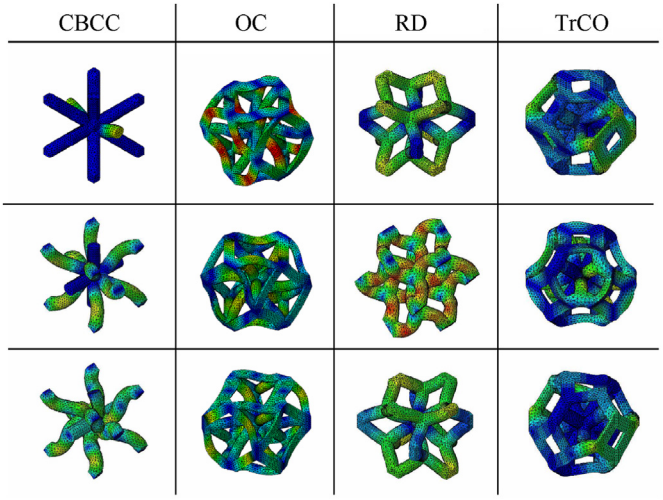

Fig. 7. Examples of three buckling modes (number 3, 6 and 8) of the four RVE geometries.

5. Numerical results

The computation of the normalized internal energy $\overline{IE}$ is performed by means of dedicated post-processing Python scripts, which are executed after those used to generate the FE models of the RVEs and to run the simulations. Abaqus automatically computes the values of the internal energy, according to Eq. (3), for each element constituting the FE model. By performing a sum over the elements constituting the FE model, the value of $\overline{IE}$ is computed as reported in Eq. (2). The normalized EAC $\overline{W}_c$ of Eq. (1) is obtained by extracting the value of the axial force and the equivalent compressive stress σ_c is obtained as the ratio of the axial force to the initial cell section.

To highlight the influence of geometrical imperfections on the dynamical response of RVE geometries, the results of the idealized RVE geometries are assumed as the reference ones and the results obtained with the scenarios of Table 3 are provided as percentage values with respect to the reference ones.

5.1. Nominal geometries

To provide a baseline for the simulations incorporating the

Table 3
Overview of the sensitivity analysis scenarios.

Scenario ID		Buckling modes	Global amplitude	Relative density
D1		1, 2, 3, 4, 5	1%	0.2
D2	D2-1	1, 2	1%	0.2
	D2-2	1, 2, 3, 4, 5, 6, 7, 8, 9, 10	1%	0.2
D3	D3-1	1, 2, 3, 4, 5	0.1%	0.2
	D3-2	1, 2, 3, 4, 5	5%	0.2
D4	D4-1	1, 2, 3, 4, 5	1%	0.4
	D4-2	1, 2, 3, 4, 5	1%	0.6

geometrical defects, a first numerical campaign of analyses is carried out on the RVE geometries without defects. The values of $\overline{IE}$ obtained for the nominal RVE geometries are reported in Fig. 8.

These results point out that the values of $\overline{IE}$ increase with the strain rate, as expected, in the same fashion for the four RVE geometries in the considered range of strain rate. This behavior is obtained also for those simulations involving greater values of relative density. It is noteworthy that when increasing the value of relative density the increase of the value of $\overline{IE}$ is not the same for all the lattice cells. As illustrated in Fig. 8, the CBCC and the TrCO geometries exhibit a higher capacity of absorbing energy within the considered range of both $\dot{\varepsilon}$ and $\overline{\rho}$. In particular, when small values of $\overline{\rho}$ are considered, the CBCC geometry proves to be the best solution. Conversely, when higher values of $\overline{\rho}$ are considered, the TrCO geometry exhibits the highest $\overline{IE}$ among the considered RVE geometries.

As introduced in Section 2, an alternative approach to evaluate the EAC, which is easily applicable in experiments, consists of computing the value of $\overline{W}_c$. As an example, Fig. 9 illustrates the longitudinal force vs. longitudinal deformation curves, extracted at the reference point of the FE model used to drive the macroscopic strain applied to the RVE FE models. By applying Eq. (1), the values of $\overline{W}_c$ can be computed for the considered RVE geometries. Fig. 10 shows the percent relative error obtained by considering the values of $\overline{IE}$ and the values of $\overline{W}_c$ resulting from the numerical analyses, whose curves are shown in Fig. 9, for a relative density equal to 0.2 and a strain rate equal to $\dot{\varepsilon} = 750\ s^{-1}$ for all the RVE geometries (the results are reported for all the strain rate values only for the TrCO geometry in Fig. 10(b)). As expected, from the energy balance of Eqs. (1) and (3), the computed values of $\overline{W}_c$ are very close to those reported in Fig. 8 with a maximum percent relative error around 3%.

5.2. Geometries with manufacturing process-induced geometrical imperfections

To investigate the effect of geometrical imperfections on the dynamical response of the considered RVE geometries, the FE models used in the simulations presented in subsection 5.1 have been modified by introducing geometrical imperfections according to the defect scenarios presented in Table 3. Greater relevance will be given to the results of the TrCO lattice geometry since, as shown later in this section, it exhibits the most efficient response, in terms of EAC, when geometrical imperfections are included within the numerical simulations. Finally, to point out the influence of geometrical imperfections on the EAC of the considered RVE geometries, most of the results presented in this section, are normalized with the counterparts obtained for the nominal RVE geometries discussed in subsection. 5.1.

An overview of the change of $\overline{IE}$ due to the presence of geometrical imperfections (for each scenario listed in Table 3) is illustrated in Fig. 11 for those RVE configurations characterized by $\overline{\rho} = 0.2$. The values of Fig. 11 represent the relative error, in percentage, with respect to the nominal values of $\overline{IE}$ shown in Fig. 8. A first analysis of these results highlights that, regardless of the strain rate value, CBCC and OC geometries are remarkably more sensitive to the presence of geometrical defects with a maximum relative

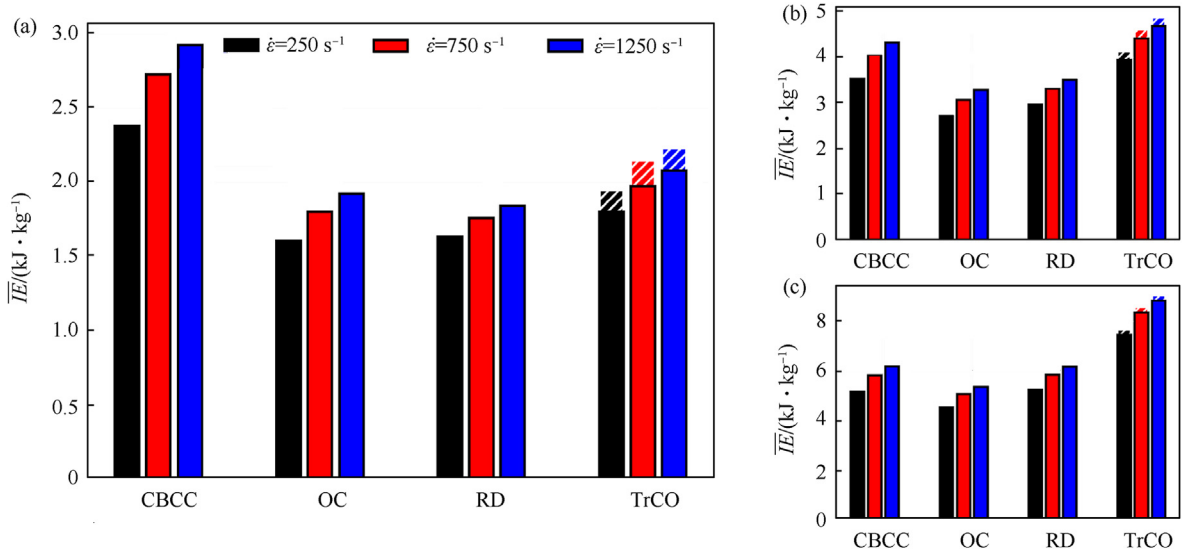

Fig. 8. Normalized strain energies of the nominal RVE geometries for three values of strain rate and three densities: (a) $\overline{\rho} = 0.2$; (b) $\overline{\rho} = 0.4$; (c) $\overline{\rho} = 0.6$. The hatched bars for the TrCO cell correspond to the values obtained with the simulations including the rigid planes, as presented in section 4.

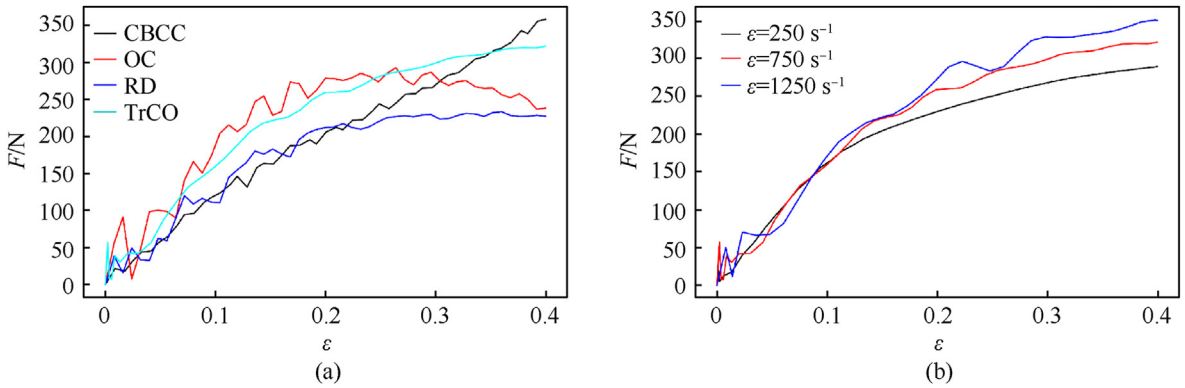

Fig. 9. (a) Longitudinal force vs. longitudinal deformation of the four considered RVE geometries with $\overline{\rho} = 0.2$ and $\dot{\varepsilon} = 750\ s^{-1}$; (b)Longitudinal force vs. longitudinal deformation of the TrCO geometry with $\overline{\rho} = 0.2$ and $\dot{\varepsilon} = [250, 750, 1250]\ s^{-1}$.

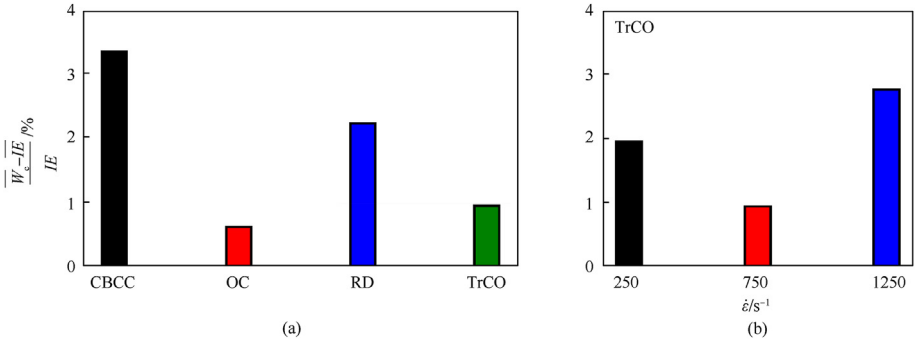

Fig. 10. Percentage error between $\overline{W}_c$ and $\overline{IE}$ for: (a)The studied lattice cells with $\overline{\rho} = 0.2$ and $\dot{\varepsilon} = 750\ s^{-1}$; (b) The TrCO lattice cell with $\overline{\rho} = 0.2$ and $\dot{\varepsilon} = [250, 750, 1250]\ s^{-1}$.

reduction of the $\overline{IE}$ reaching values of about 50%. Conversely, RD and the TrCO geometries exhibit a less significant modification in the $\overline{IE}$ values with percentage differences ranging between, approximately, 1% and 17%.

The influence of the different scenarios (for $\overline{\rho} = 0.2$, scenarios D1, D2-1, D2-2, D3-1 and D3-2) can be observed on the magnitude of the reduction of $\overline{IE}$. If scenario D1 is assumed as reference (black bars in Fig. 11), by keeping unchanged the global amplitude of the defect, when a smaller number of modes (scenario D2-1) is used to generate the imperfection, a greater reduction (red bars in Fig. 11) is obtained. Conversely, by increasing the number of modes, the value of relative error (blue bars in Fig. 11) is essentially equal to the that obtained with the scenario D1. As a matter of fact, when the number of modes is excessively small, the structural instabilities undergone by the RVE geometries take place for a smaller macroscopic deformation. This pattern can be observed for the CBCC, OC and RD geometries for all the considered strain rate values while the TrCO geometry seems to be almost insensitive to the choice of the number of modes.

From the analysis of the results illustrated in Fig. 11 one can infer that for all the RVE geometries and for all the simulated strain rate values, the smaller the imperfections (scenario D3-1) the smaller the reduction of the $\overline{IE}$ (green bars in Fig. 11) and, when the

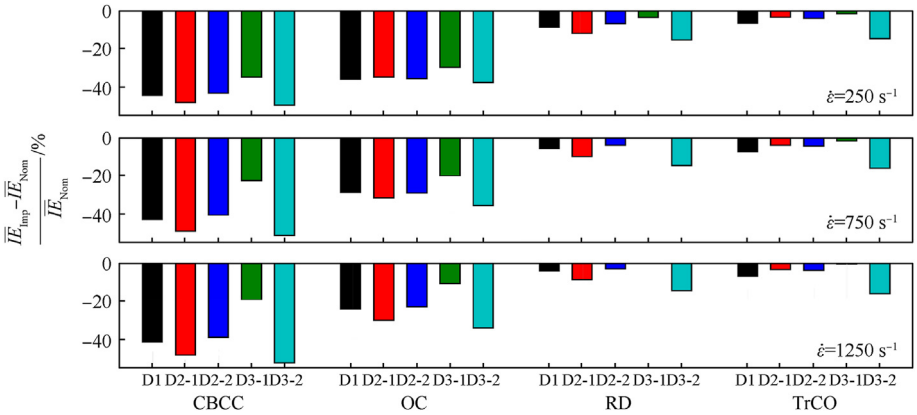

Fig. 11. Percentage error of the values of $\overline{IE}_{Imp}$ computed for the different scenarios of Table 3 (for the RVE geometries characterized by $\overline{\rho} = 0.2$) with respect to the corresponding values obtained with the nominal RVE geometries, $\overline{IE}_{Nom}$.

magnitude is increased as in scenario D3-2, the maximum reduction in $\overline{IE}$ is attained (cyan bars in Fig. 11).

A deeper insight of the results shown in Fig. 11 can be gained by observing the longitudinal force vs. longitudinal deformation when geometrical imperfections are included into the analysis. Specifically, Fig. 12 illustrates the comparison between the scenario with no geometrical defect (continuous lines) and the scenario D1 (dashed lines) for the four RVE geometries at $\dot{\varepsilon} = 750\ s^{-1}$. As already discussed for the values of relative error of Fig. 11, CBCC and OC geometries are remarkably sensitive to the presence of a small geometrical defect, with a sudden force reduction at approximately $\varepsilon = 0.15$. This behavior is probably due to the presence of struts aligned to direction of compression which, without introducing defects, undergo solely axial compression and, when defects are introduced, they undergo a combination of axial compression and bending. For RD and TrCO geometries, the reduction of the force is less significant and the macroscopic deformation, after which the difference between the curves is higher, shifts at a value greater than $\varepsilon = 0.2$. By observing the results relative to the RVE geometries characterized by $\overline{\rho} = 0.2$ of Figs. 11 and 12 and by considering the reduction of $\overline{IE}$ with respect to the results of Fig. 8, the TrCO geometry proves to be, within the limits of the hypotheses at the basis of the numerical analyses, the most efficient configuration, in terms of $\overline{IE}$, when a realistic magnitude of geometrical defect is assumed.

The influence of the number of modes included in the generation of the defect and of its magnitude, as well as the strain-rate effects, can also be observed on the curves representing the longitudinal force vs. longitudinal deformation in Fig. 13. If scenario D1 is assumed as reference, a greater defect (scenario D3-2) shifts the curves towards smaller values of the longitudinal force (green curves in Fig. 13) while smaller values (scenario D3-1) makes the

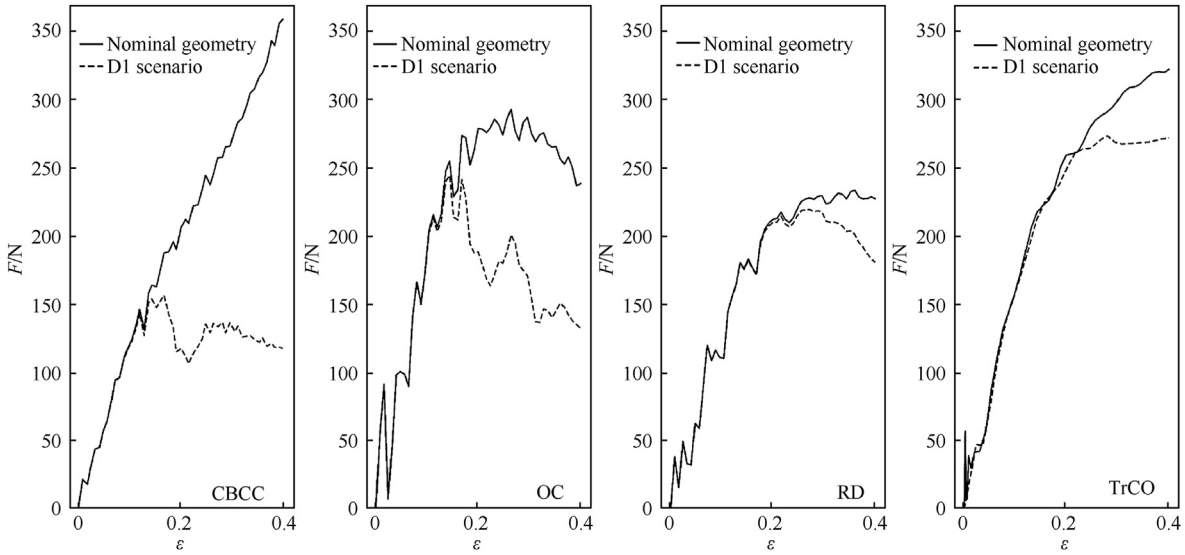

Fig. 12. Comparison between the longitudinal force vs. longitudinal deformation of the four RVE geometries for $\overline{\rho} = 0.2$ and $\dot{\varepsilon} = 750\ s^{-1}$ between nominal geometries and those of the D1 scenario.

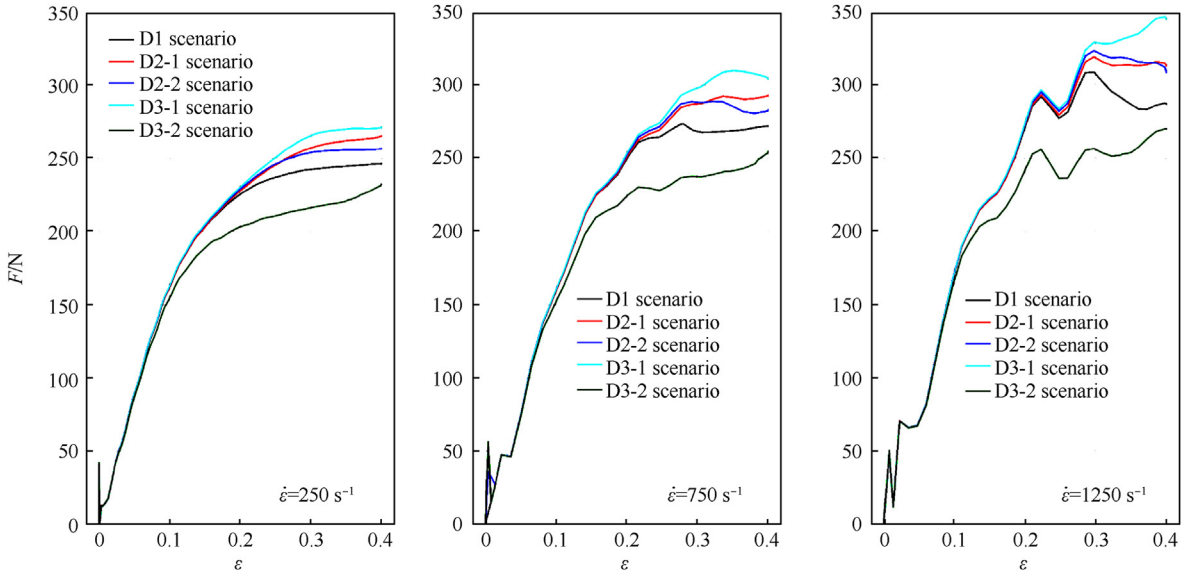

Fig. 13. Comparison between the longitudinal force vs. longitudinal deformation for the TrCO geometry between the scenarios of Table 3 carried out with $\overline{\rho} = 0.2$ and $\dot{\varepsilon} = [250, 750, 1250]\ s^{-1}$.

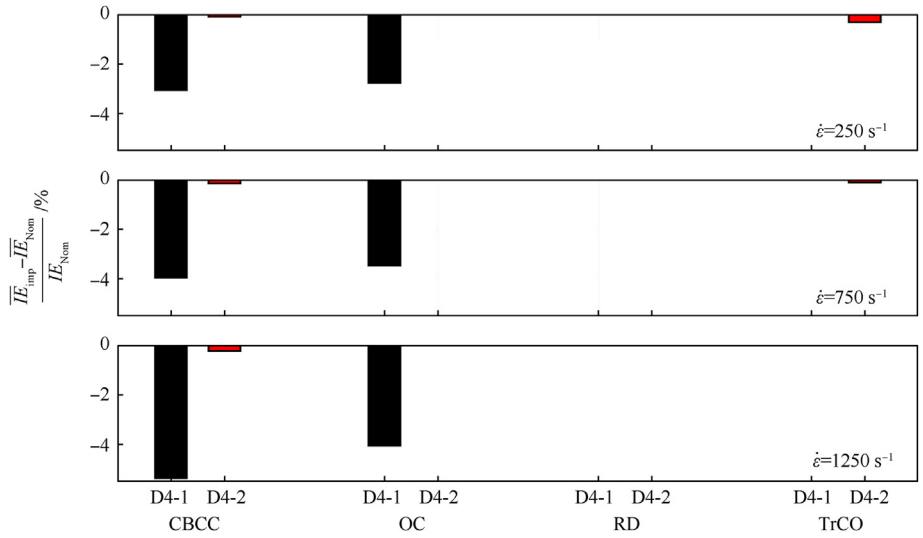

Fig. 14. Percentage error between $\overline{IE}_{Imp}$ and $\overline{IE}_{Nom}$ for all RVE geometries by considering scenarios D4-1 and D4-2 of Table 3 and $\dot{\varepsilon} = [250, 750, 1250]$ s^{-1}.

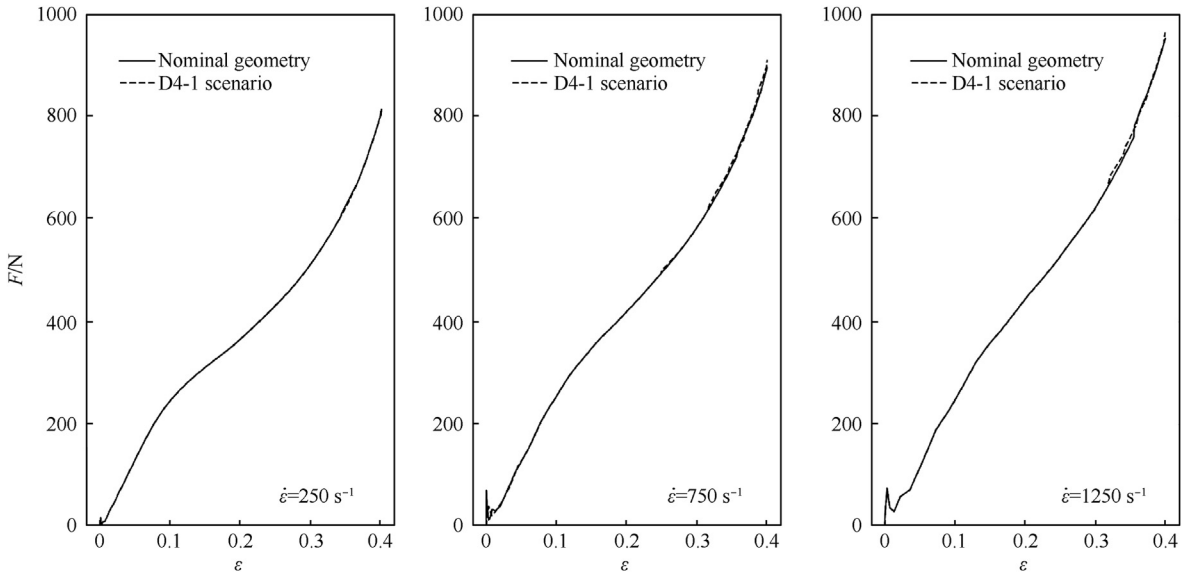

Fig. 15. Comparison between the longitudinal force vs. longitudinal deformation of the TrCO geometry for the D4-1 scenario of Table 3 carried out with $\overline{\rho} = 0.4$ and $\dot{\varepsilon} = [250, 750, 1250]$ s^{-1}.

TrCO geometry closer to the nominal one with a consequent increase of longitudinal force (cyan curves in Fig. 13).

If compared to the other RVE geometries, the TrCO topology exhibits a distinct mechanical response when different number of modes are used to generate the geometrical defect (by keeping constant the amplitude of the defect). In fact, unlike the behavior of the other RVE geometries, the values of longitudinal force of scenario D2-1 (where only two modes are used to generate the defect) are in any case greater than those obtained with the scenario D1. This response is probably due to the specific influence of these two buckling modes, used to create the geometrical imperfection, on the deformation of the TrCO geometry.

The results of the numerical analyses including geometrical defects for the RVE geometries characterized by values of relative density equal to $\overline{\rho} = 0.4$ and $\overline{\rho} = 0.6$, are shown in Fig. 14, where the percentage errors between the simulations including defects, i.e., scenarios D4-1 and D4-2, and those considering the nominal geometries are reported. It stands out that all the RVE geometries are remarkably less sensitive to defects with maximum relative errors smaller than 5% for the CBCC and OC geometries characterized by $\overline{\rho} = 0.4$ and significantly even smaller values (less than 0.5%) for all the other studied cases. As an example, these results can also be interpreted on the basis of the longitudinal force vs. longitudinal deformation curves of Figs. 15 and 16, extracted from the numerical analyses of the TrCO geometry at $\overline{\rho} = 0.4$ and $\overline{\rho} = 0.6$, respectively. Due to the greater values of relative density, the magnitude of the geometrical defect is not capable of triggering different instabilities of the struts constituting the RVE compared to the simulations on the nominal geometries. Of course, for these values of relative density the presence of a geometrical defect would be detectable only if a significant magnitude of the defect is included in the simulations.

Finally, the comparison between the values of $\overline{IE}$ and $\overline{W}_c$, the latter computed via Eq. (1), of the numerical analyses including

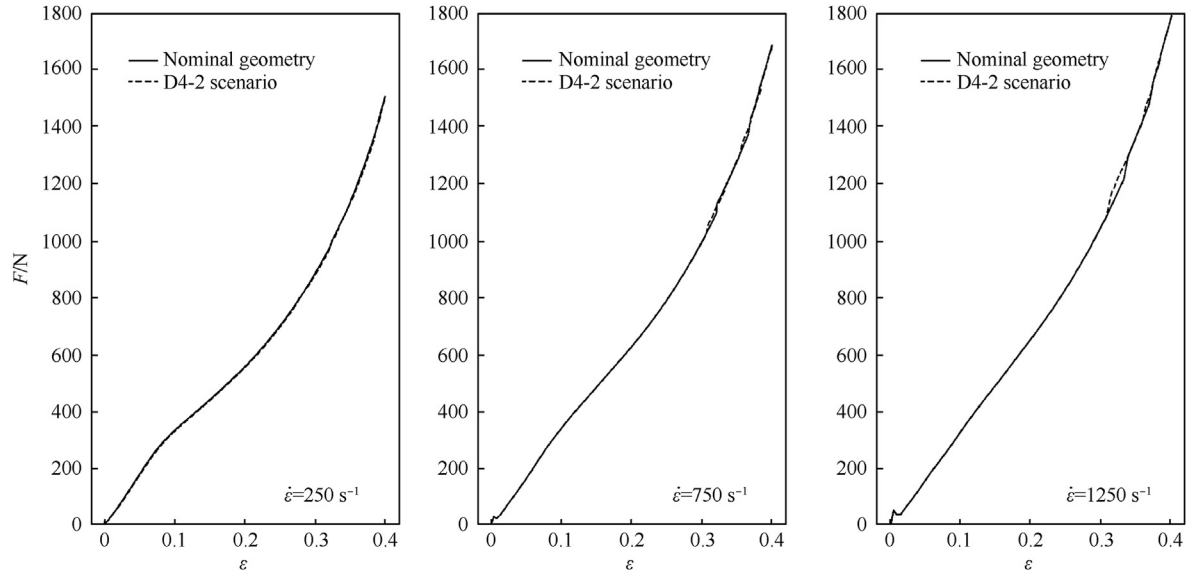

Fig. 16. Comparison between the longitudinal force vs. longitudinal deformation of the TrCO geometry for the D4-2 scenarios of Table 3 carried out with $\overline{\rho} = 0.6$ and $\dot{\varepsilon} = [250, 750, 1250]$ s^{-1}.

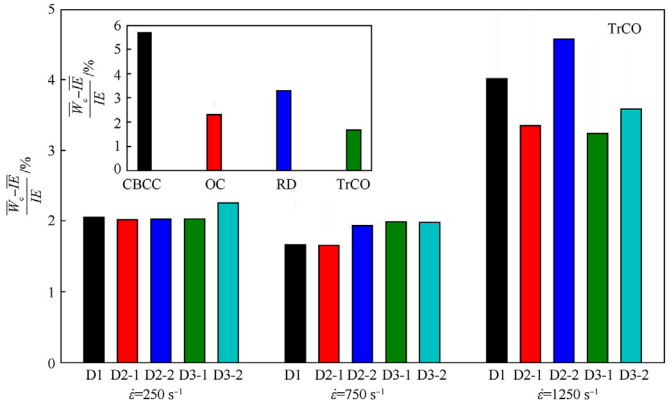

Fig. 17. Percentage error between $\overline{W}_c$ and $\overline{IE}$ obtained from the force vs deformation curves of Figs. 12 and 13.

imperfections and characterized by a value of relative density $\overline{\rho} = 0.2$, are shown in Fig. 17. The results show that both indicators return consistent values. Among the considered RVE geometries and defect scenarios, the maximum value of the relative error, which is about 6%, is obtained for the CBCC geometry. For all the other lattice geometries and defect scenarios, the relative errors range between 1.6% and 5%, approximately.

6. Conclusions

In this study, the influence of geometrical defects on the energy absorption capacity and on the dynamical response of four lattice structure geometries, by considering different relative densities, subject to uni-axial strain field at different strain-rate values has been investigated. This study contributes to develop a numerical framework aimed at addressing the energy absorption of lattice structures for real-life shock absorption applications.

Particularly, the study of geometrical defects, typically obtained in additive manufacturing processes of polymers, allows to consider, within the design phase, the reduction in terms of energy absorption capacity that, for certain geometries, can be significant.

Non-linear numerical analyses have been performed by considering non-linear, strain rate-dependent material behavior together with contact interactions between the struts of the lattice structures and between different cells to reproduce, through a dedicated modeling strategy developed for a single representative volume element, the beginning of the densification phase.

A broad range of defect scenarios has been investigated where the magnitude and the global shape of the defect have been selected as the main parameters to be modified during the sensitivity analysis. (1) The results indicate that when considering nominal geometries (i.e., without introducing defects) the energy absorption capacity is significantly dependent on the lattice geometry with the CBCC being the most efficient geometry at small density and the TrCO being the most efficient one at higher densities; (2) the introduction of defects induces a reduction in energy absorption capacity, for the lattice cells characterized by $\overline{\rho} = 0.2$, which is remarkable (between 20% and 50% of the values obtained with no defects) for CBCC and OC configurations and it is significantly smaller for RD and TrCO geometries (between 1% and 16%); (3) the geometries characterized by a greater value of relative density ($\overline{\rho} = 0.4$ and $\overline{\rho} = 0.6$) are essentially insensitive to the presence of the simulated defects.

Even though these results are limited to uni-axial strain field and to a limited number of lattice geometries, they highlight that it is questionable to consider geometrically perfect lattice geometries when dealing with the assessment of the energy absorption capacity of lattice structures. Ongoing studies are addressing more complex loading conditions, a larger number of lattice geometries as well as evaluating if, with canonical geometries, it is possible to optimize their response by acting on the geometrical parameters defining the lattice cell. To further advance the design of lattice structures, the use of robust design strategies would also promote a better understanding of the effects of sources of uncertainty on the structural response. This will require extensive experimental campaigns to measure both the relevant material properties and the associated scattering to be used in numerical analyses. Of course, when numerical analyses of large lattice structures are

needed, it would be impractical to explicitly model every single lattice cell of the structure. To this end, non-linear homogenization techniques are of paramount importance and should be applied, on lattice structures including geometrical imperfections.

Declaration of competing interest

The authors declare that they have no known competing financial interests or personal relationships that could have appeared to influence the work reported in this paper.

Acknowledgments

A. Riot is grateful to the CEA (Comissariat à l'Energie Atomique et aux Energies Alternatives) and the DGA (Direction Générale de l'Armement) for providing financial support.

References

[1] Gibson L, Ashby M. Cellular solids : structures and properties. Cambridge Solid State Science Series; 1999.
[2] Sanchez-Saez S, Barbero E, Garcia-Castillo S, Ivanez I, Cirne J. Experimental response of agglomerated cork under multi-impact loads. Mater Lett 2015;160:327–30.
[3] Ivanez I, Sanchez-Saez S, Garcia-Castillo S, Barbero E, Amaro A, Reis P. High-velocity impact behaviour of damaged sandwich plates with agglomerated cork core. Compos Struct 2020;248:112520.
[4] Coelho R, Alves de Sousa R, Fernandes F, Teixeira-Dias F. New composite liners for energy absorption purposes. Mater Des 2013;43:384–92.
[5] Samlal S, Santhanakrishnan R, Paulson V, Goyal C. Flexural property evaluation of foam core sandwich panel with carbon/kevlar epoxy hybrid facesheets. Mater Today: Proceedings 2020. https://doi.org/10.1016/j.matpr.2020.09.347.
[6] Marsavina L, Sadowski T, Kne'c M, Negru R. Non-linear behaviour of foams under static and impact three point bending. Int J Non Lin Mech 2010;45(10):969–75. https://doi.org/10.1016/j.ijnonlinmec.2010.03.007. special Issue on "Nonlinear mechanics of modern materials".
[7] Zhang Q, Lu W, Scarpa F, Barton D, Lakes R, Zhu Y, Lang Z, Peng H-X. Large stiffness thermoformed open cell foams with auxeticity. Appl Mater Today 2020;20:100775.
[8] Bloodworth-Race S, Critchley R, Hazael R, Peare A, Temple T. Testing the blast response of foam inserts for helmets. Heliyon 2021;7:e06990.
[9] Notario P, Pinto J, Solorzano E, de Saja J, Dumon M, Rodriguez-P'erez M. Experimental validation of the knudsen effect in nanocellular polymeric foams. Polymer 2015;56:57–67.
[10] Liu Y, Rahimidehgolan F, Altenhof W. Anisotropic compressive behavior of rigid pvc foam at strain rates up to 200 s-1. Polym Test 2020;91:106836.
[11] Wu Y, Sun L, Yang P, Fang J, Li W. Energy absorption of additively manufactured functionally bi-graded thickness honeycombs subjected to axial loads. Thin-Walled Struct 2021;164:107810.
[12] Robinson M, Soe S, Johnston R, Adams R, Hanna B, Burek R, McShane G, Celeghini R, Alves M, Theobald P. Mechanical characterisation of additively man- ufactured elastomeric structures for variable strain rate applications. Addit Manuf 2019;27:398–407.
[13] Montemurro M, Catapano A, Doroszewski D. A multi-scale approach for the simultaneous shape and material optimisation of sandwich panels with cellular core. Compos B Eng 2016;91:458–72.
[14] Montemurro M, Refai K, Catapano A. Thermal design of graded architected cel- lular materials through a cad-compatible topology optimisation method. Compos Struct 2022;280:114862. https://10.1016/j.compstruct.2021.114862.
[15] Bates S, Farrow I, Trask R. 3d printed polyurethane honeycombs for repeated tailored energy absorption. Mater Des 2016;112:172–83.
[16] hua Dong J, jun Wang Y, nian Jin F, lin Fan H. Crushing behaviors of buckling-induced metallic meta-lattice structures. Defence Technology 2022;18(8):1301–10.
[17] zhu Feng G, Wang J, yuan Li X, jun Xiao L, dong Song W. Mechanical behavior of ti–6al–4v lattice-walled tubes under uniaxial compression. Defence Technology 2022;18(7):1124–38.
[18] chen Wei Y, jie Tian M, yang Huang C, wu Wang S, Li X, ran Hu Q, qi Yuan M. Topological study about failure behavior and energy absorption of honeycomb structures under various strain rates. Defence Technology 2022. https://doi.org/10.1016/j.dt.2022.03.011.
[19] Duan S, Wen W, Fang D. Additively-manufactured anisotropic and isotropic 3d plate-lattice materials for enhanced mechanical performances: simulations & experi- ments. Acta Mater 2020;199:397–412.
[20] Refai K, Brugger C, Montemurro M, Saintier N. An experimental and numerical study of the high cycle multiaxial fatigue strength of titanium lattice structures produced by Selective Laser Melting (SLM). Int J Fatig 2020;138:105623.
[21] Montemurro M, Bertolino G, Roiné T. A general multi-scale topology optimisation method for lightweight lattice structures obtained through additive manufacturing technology. Compos Struct 2021;258:113360.
[22] Bertolino G, Montemurro M. Two-scale topology optimisation of cellular materials under mixed boundary conditions. Int J Mech Sci 2022;216:106961. https://doi.org/10.1016/j.ijmecsci.2021.106961.
[23] Montemurro M, Roiné T, Pailhès J. Multi-scale design of multi-material lattice structures through a CAD-compatible topology optimisation algorithm. Eng Struct 2022;273:115009. https://doi.org/10.1016/j.engstruct.2022.115009.
[24] Li D, Liao W, Dai N, X YM. Comparison of mechanical properties and energy absorption of sheet-based and strut-based gyroid cellular structures with graded den- sities. Materials 2019;12:2183.
[25] Hundley J, Clough E, Jacobsen A. The low velocity impact response of sandwich panels with lattice core reinforcement. Int J Impact Eng 2015;84:64–77.
[26] Habib F, Iovenitti S, Masood S, Nikzad M. Fabrication of polymeric lattice struc- tures for optimum energy absorption using multi jet fusion technology. Mater Des 2018;155:86–98.
[27] Nasim M, Hasan MJ, Galvanetto U. Impact behavior of energy absorbing helmet liners with pa12 lattice structures: a computational study. Int J Mech Sci 2022;233:107673. https://doi.org/10.1016/j.ijmecsci.2022.107673.
[28] Clough E, Plaisted T, Eckel Z, Cante K, Hundley J, Schaedler T. Elastomeric microlattice impact attenuators. Matter 2019;1:1519–31.
[29] Sun Z, Guo Y, Shim V. Characterisation and modeling of additively-manufactured polymeric hybrid lattice structures for energy absorption. Int J Mech Sci 2020. https://doi.org/10.1016/j.ijmecsci.2020.106101.
[30] Bai L, Gong C, Chen X, Sun Y, Xin L, Pu H, Peng Y, Luo J. Mechanical properties and energy absorption capabilities of functionally graded lattice structures: experiments and simulations. Int J Mech Sci 2020;182:105735.
[31] Jiang W, Yin G, Xie L, Yin M. Multifunctional 3d lattice metamaterials for vibra- tion mitigation and energy absorption. Int J Mech Sci 2022;233:107678. https://doi.org/10.1016/j.ijmecsci.2022.107678.
[32] Liang H, Sun B, Hao W, Sun H, Pu Y, Ma F. Crashworthiness of lantern-like lattice structures with a bidirectional gradient distribution. Int J Mech Sci 2022:107746. https://doi.org/10.1016/j.ijmecsci.2022.107746.
[33] Chen L, Zhang J, Du B, Zhou H, Liu H, Guo Y, Li W, Fang D. Dynamic crushing behavior and energy absorption of graded lattice cylindrical structure under axial impact load. Thin-Walled Struct 2018;127:333–43.
[34] Markou A, St-Pierre L. A novel parameter to tailor the properties of prismatic lattice materials. Int J Mech Sci 2022;219:107079. https://doi.org/10.1016/j.ijmecsci.2022.107079.
[35] Dong G, Tang Y, Zhao Y. A survey of modeling of lattice structures fabricated by additive manufacturing. J Mech Des 2017;139(10):100906. https://doi.org/10.1115/1.4037305.
[36] Tao W, Leu MC. Design of lattice structure for additive manufacturing. In: 2016 International Symposium on Flexible automation (ISFA); 2016. p. 325–32. https://doi.org/10.1109/ISFA.2016.7790182.
[37] Mahmoud D, Elbestawi MA. Lattice structures and functionally graded materials applications in additive manufacturing of orthopedic implants: a review. Journal of Manufacturing and Materials Processing 2017;1(2). https://doi.org/10.3390/jmmp1020013.
[38] Gonzalez-Henriquez C, Sarabia-Vallejos M, Rodriguez-Hernandez J. Polymers for additive manufacturing and 4d-printing: materials,methodologies, and biomedical applications. Prog Polym Sci 2019;94:57–116.
[39] Torre R, Brischetto S. Experimental characterization and finite element validation of orthotropic 3d-printed polymeric parts. Int J Mech Sci 2022;219:107095. https://doi.org/10.1016/j.ijmecsci.2022.107095.
[40] Schmutzler C, Zimmermann A, Zaeh M. Compensating warpage of 3d printed parts using free-form deformation. In: 48th CIRP Conference on MANUFACTURING SYS- TEMS, Procedia CIRP; 2016. p. 1017–22. 41.
[41] Dallago M, Winiarski B, Zanini F, Carmignato S, Benedetti M. On the effect of geometrical imperfections and defects on the fatigue strength of cellular lattice structures additively manufactured via selective laser melting. Int J Fatig 2019;124:348–60.
[42] Barati M, Zenkour A. Investigating post-buckling of geometrically imperfect metal foam nanobeams with symmetric and asymmetric porosity distributions. Compos Struct 2017;182:91–8.
[43] Martins A, Silvestre N. Modal analysis and imperfection sensitivity of the post-buckling behaviour of cylindrical steel panels under in-plane bending. Eng Struct 2020;207:110127.
[44] Kladovasilakis N, Tsongas K, Karalekas D, Tzetzis D. Architected materials for additive manufacturing: a comprehensive review. Materials 2022;15(17). https://doi.org/10.3390/ma15175919.
[45] Maconachie T, Leary M, Lozanovski B, Zhang X, Qian M, Faruque O, Brandt M. Slm lattice structures: properties, performance, applications and challenges. Materi- als & Design 2019;183:108137. https://doi.org/10.1016/j.matdes.2019.108137.
[46] Harris J, Winter R, McShane G. Impact response of additively manufactured metal- lic hybrid lattice materials. Int J Impact Eng 2017;104:177–91.
[47] Abayazid F, Ghajari M. Material characterisation of additively manufactured elas- tomers at different strain rates and build orientations. Addit Manuf 2020;33:101160.
[48] Jamil A, Guan Z, Cantwell W, Zhang X, Langdon G, Wang Q. Blast response of aluminium/thermoplastic polyurethane sandwich panels – experimental work and numerical analysis. Int J Impact Eng 2019;127:31–40.
[49] Lejeunes S, Bourgeois S. Une toolbox abaqus pour le calcul de propriétés effectives de milieux hétérogènes. In: CSMA, 10e Colloque Nationale en Calcul des Structures; 2011. p. 1–8.

[50] Corp DSS. ABAQUS/Standard analysis User's Guide. 2021. Version 2021.
[51] Boni L, Fanteria D, Lanciotti A. Post-buckling behaviour of flat stiffened composite panels: experiments vs. analysis. Compos Struct 2012;94(12): 3421–33. https://doi.org/10.1016/j.compstruct.2012.06.005.
[52] Prato A, Al-Saymaree M, Featherston C, Kennedy D. Buckling and post-buckling of thin-walled stiffened panels: modelling imperfections and joints. Thin-Walled Struct 2022;172:108938. https://doi.org/10.1016/j.tws.2022.108938.
[53] Martins AD, Silvestre N. Modal analysis and imperfection sensitivity of the post- buckling behaviour of cylindrical steel panels under in-plane bending. Eng Struct 2020;207:110127. https://doi.org/10.1016/j.engstruct.2019.